Letter

Efficient generation of tunable magnetic and optical vortices using plasmas

Yipeng Wu,[1,*] Xinlu Xu,[2] Chaojie Zhang,[1] Zan Nie,[1] Mitchell Sinclair,[1] Audrey Farrell,[1] Kenneth A. Marsh,[1] Jianfei Hua,[3] Wei Lu,[3] Warren B. Mori,[1,4] and Chan Joshi[1,†]

[1]*Department of Electrical and Computer Engineering, University of California, Los Angeles, California 90095, USA*
[2]*SLAC National Accelerator Laboratory, Stanford, California 94309, USA*
[3]*Department of Engineering Physics, Tsinghua University, Beijing 100084, China*
[4]*Department of Physics and Astronomy, University of California, Los Angeles, California 90095, USA*

(Received 13 April 2022; revised 11 August 2022; accepted 2 January 2023; published 27 January 2023)

Plasma is an attractive medium for generating strong microscopic magnetic structures and tunable electromagnetic radiation with predictable topologies due to its extraordinary ability to sustain and manipulate high currents and strong fields. Here, using theory and simulations, we show efficient generation of multimegagauss magnetic and tunable optical vortices when a sharp relativistic ionization front (IF) passes through a relatively long wavelength Laguerre-Gaussian (LG) laser pulse with orbital angular momentum (OAM). The optical vortex is frequency upshifted within a wide spectral range simply by changing the plasma density and is compressed in duration. The topological charges of both vortices can be manipulated by controlling the OAM mode of the incident LG laser and/or by controlling the topology and density of the IF. For relatively high (low) plasma densities, most of the energy of the incident LG laser pulse is converted into the magnetic (optical) vortex, with conversion efficiency approaching ∼90% for an ideal IF.

DOI: 10.1103/PhysRevResearch.5.L012011

Magnetic fields play an important role in numerous areas ranging from condensed matter physics [1] and accelerator and beam physics to nuclear fusion [2] and astrophysics [3]. As these fields rapidly grow, ultrastrong (megagauss level or even higher) magnetic fields with various topologies are becoming desirable. Laser-plasma interactions have the potential to produce such fields. Therefore much effort has been devoted to the generation of plasma-based magnetic structures with different topologies, such as dc axial magnetic fields [4–10], surface magnetic fields [11–13], and planar periodic magnetic fields [14–16]. Despite this progress, it is not yet possible to precisely control the azimuthal degree of freedom of these fields.

Here, we show using theory and three-dimensional (3D) particle-in-cell (PIC) simulations that a multimegagauss magnetic vortex with a helical structure can be efficiently generated when a Laguerre-Gaussian (LG) laser carrying orbital angular momentum (OAM) interacts with a counterpropagating relativistic ionization front (IF). The topology of this spatially periodic but zero-frequency magnetic field can be manipulated by controlling the OAM mode of the LG laser and the topology of the IF, while the strength of the field can be varied by changing the plasma density. This magnetostatic structure is not only a fundamental mode of the plasma, but also important in applications such as topological quantum system manipulation [17]. Also as we shall see later, such magnetic structures could be used as ultracompact spiral undulators (approximately micrometer period) for generating coherent ∼1-nm x rays with OAM using planarly bunched electron beams with energy of just a few tens of MeV, compared with the case of conventional permanent-magnet planar undulators (approximately centimeter period) where multi-GeV helically bunched electron beams are required [18,19]. This could pave the way for the next-generation ultracompact OAM x-ray sources.

In addition, upon collision with the IF, the LG laser is frequency upshifted due to the relativistic Doppler effect and compressed since the number of optical cycles is conserved. The resulting wavelength can be tuned by varying the plasma density. The OAM mode of the upshifted light can be manipulated either by changing the OAM mode of the incident LG pulse or by tuning the density and topology of the IF. Such OAM- and frequency-tunable optical vortices can be used in a diverse array of research disciplines, including optical manipulation [20,21], generation of high-order harmonics carrying OAM [22–25], fabrication of chiral organic materials [26,27], and high-capacity optical communication using wavelength-division and OAM-mode-division multiplexing [28]. Although there exist some conventional OAM-tuning optical elements, such as spiral phase plates [29], q plates [30,31], and spatial light modulators [32], few can realize OAM and frequency tuning simultaneously, especially with a wide tunable range. We note that the frequency upshifting of a nonvortex electromagnetic wave or periodic electrostatic field using a planar IF has been theoretically studied [14,15,33–37] and experimentally demonstrated in the microwave [38–44] and optical [45,46] regimes. However, neither the OAM

*wuyipeng@ucla.edu
†cjoshi@ucla.edu

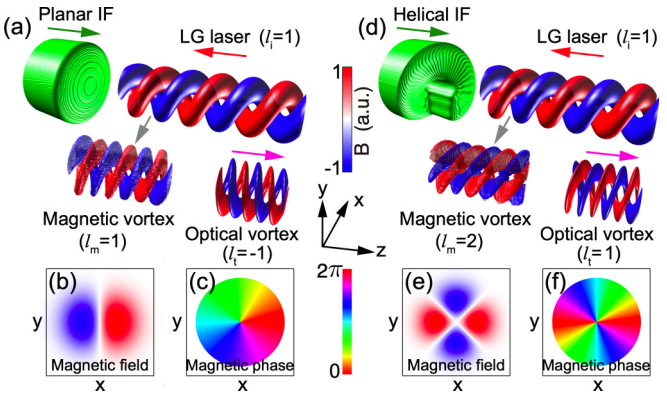

FIG. 1. Generation of a magnetic or optical vortex through the interaction of a LG laser pulse with a planar (a) or helical (d) relativistic IF. The field distributions of the magnetic vortex at a particular z are shown in (b) (planar IF) and (e) (helical IF). The corresponding phase distributions of the magnetic vortex are shown in (c) (planar IF) and (f) (helical IF).

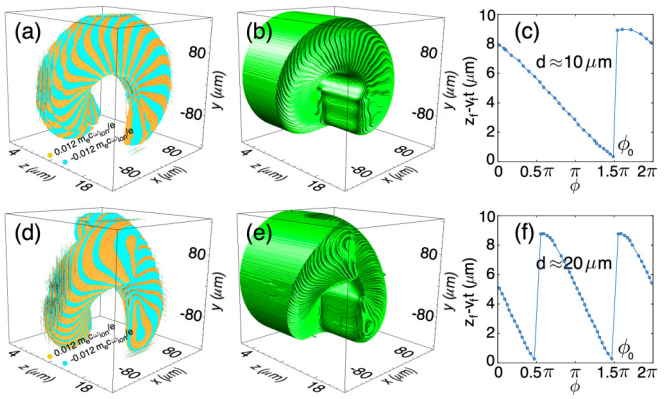

FIG. 2. (a) and (d) Simulated isosurfaces of the LS electric field. (b) and (e) Density isosurfaces of the helical IF. (c) and (f) The IF position z_f vs ϕ. (a)–(c) are for the the first-order LS composed of $LG_{0,1}$ and $LG_{0,2}$ modes. (d)–(f) are for the second-order LS consisting of $LG_{0,-1}$ and $LG_{0,1}$ modes. In both cases, the wavelengths of the two LG modes are 407 and 393 nm. The other parameters are presented in the Supplemental Material, Note 1.

degree of freedom nor topological control of the IF was involved in these works.

To gain a deeper insight into the generation of magnetic and optical vortices, we first carry out a theoretical analysis. The basic concept is schematically shown in Fig. 1. Here a linearly x-polarized LG_{p_i,l_i} laser with a wavelength of λ_i, an azimuthal mode index (also called topological charge) of l_i, and zero radial mode index ($p_i = 0$) is incident from the right on a planar [Fig. 1(a)] or helical [Fig. 1(d)] relativistic IF. The IF is generated via optical field ionization of neutral gas by a linearly y-polarized femtosecond laser pulse and moves to the right with velocity $v_f \sim c$. Ahead of the IF is un-ionized gas, while behind the IF is plasma. Considering the interaction within the Rayleigh length and thus neglecting the Gouy phase effect, the electric (in the x direction) and magnetic (in the y direction) fields of the incident LG laser have a phase term $E_{i,x} = cB_{i,y} \propto \exp(-ik_i z - i\omega_i t - il_i\phi)$ [47], where $k_i = 2\pi/\lambda_i$ is the wave number, $\phi = \arctan(y/x)$ is the azimuthal angle, $\omega_i = k_i c$ is the laser frequency, and l_i gives rise to the OAM.

Here, the ionizing laser used to produce the IF is either a Gaussian pulse with a frequency of $\omega_{\rm ion} \gg \omega_i$ (planar IF) or a spatiotemporally shaped pulse called a light spring (LS) [48,49], which is obtained by superimposing copropagating LG pulses with two different frequencies ($\omega_{\rm ion} \pm \Delta\omega_{\rm ion}/2$) differing by $\Delta\omega_{\rm ion}$ and two different OAM modes differing by $\Delta l_{\rm ion}$ (helical IF). In the latter case, the intensity profile of the LS has an azimuthal beating pattern with beating frequency of $\Delta\omega_{\rm ion}$ and beating topological charge of $\Delta l_{\rm ion}$. Then the LS is referred to as being of ($|\Delta l_{\rm ion}|$)th order and consists of $|\Delta l_{\rm ion}|$ intertwined helices. In the time domain, the temporal pitch of the helix is given by $|\Delta\tau_h|$, where $\Delta\tau_h = 2\pi\,\Delta l_{\rm ion}/\Delta\omega_{\rm ion}$. Figure 2(a) shows 3D PIC simulation results with the code OSIRIS [50] of a first-order LS ($|\Delta l_{\rm ion}| = 1$) consisting of dual-frequency $LG_{0,1}$ and $LG_{0,2}$ modes (see Supplemental Material, Note 1, for detailed parameters [51]). When its peak intensity and temporal profile are properly chosen, this LS can ionize the neutral gas and generate a first-order helical IF that has azimuthally varying thickness with a sudden jump at $\phi = \phi_0$ [Fig. 2(b)]. Note that ϕ_0 is determined by the initial phase difference between the two LG modes. At any given time t, the front position z_f, defined as the longitudinal position where full ionization happens, versus the azimuthal angle ϕ is shown in Fig. 2(c). The linear dependence of z_f on ϕ can be clearly seen for most of the IF except near the thickness jump position. As we shall see later, it is this small nonlinearity that slightly influences the output OAM mode purity. The slope of this azimuthal linearity for z_f can be estimated as $-\frac{d}{2\pi}$, where $d = \alpha c\Delta\tau_h$ with α being a coefficient close to 1 (the exact value depends on the peak intensity and temporal profile of the LS and can be obtained from the simulation results).

In addition to the first-order LS, a high-order LS ($|\Delta l_{\rm ion}| > 1$) can also generate a helical IF. For example, a second-order LS ($|\Delta l_{\rm ion}| = 2$) composed of dual-frequency $LG_{0,-1}$ and $LG_{0,1}$ modes (see Supplemental Material, Note 1, for detailed parameters) is shown in Fig. 2(d). The generated high-order IF is characterized by a "split" configuration consisting of $|\Delta l_{\rm ion}|$ identical sections with a thickness step between every two sections. Each section occupies an angular region of $2\pi/|\Delta l_{\rm ion}|$ and has a quasilinear azimuthally dependent thickness [Fig. 2(e)]. Similar to the first-order IF case, the slope of z_f in each section can still be estimated as $-\frac{d}{2\pi} \approx -\alpha c\Delta l_{\rm ion}/\Delta\omega_{\rm ion}$ [Fig. 2(f)].

To simplify the following theoretical analysis, we first consider the first-order helical IF. Without loss of generality, $\phi_0 = 2\pi$ is assumed here, and thus the IF position z_f can be approximately expressed as

$$z_f(t,\phi) \approx v_f t + \frac{2\pi - \phi}{2\pi} d. \tag{1}$$

Note that although there is a slight difference between the above idealized expression and the actual case, the key physics is still preserved. As one can see, z_f decreases (increases) in the anticlockwise direction from the value $v_f t + d$ at $\phi = 0$ to the value $v_f t$ at $\phi = 2\pi$ for $d > 0$ ($d < 0$).

Equation (1) can also describe the planar IF simply by setting $d = 0$.

In order to simplify the analysis, we perform a Lorentz transformation from the laboratory frame to a new frame where the IF is a stationary boundary. In this IF frame, we denote quantities by primes. The longitudinal position of the IF becomes $z'_f(\phi') = \frac{2\pi-\phi'}{2\pi}\gamma_f d$, where $\gamma_f = (1-\beta_f^2)^{-1/2}$ and $\beta_f = v_f/c$. The plasma electrons and ions are continually emitted from the IF boundary to the left with velocity v_f. The incident wave is Doppler upshifted to $E'_{i,x} \propto \exp(-ik'_i z' - i\omega'_i t' - il'_i\phi')$, with $\omega'_i = (1+\beta_f)\gamma_f\omega_i$, $l'_i = l_i$, and $k'_i = \omega'_i/c$, while the plasma frequency is still $\omega_p \equiv \sqrt{\frac{n_p e^2}{m_e\epsilon_0}}$ since it is a Lorentz invariant, with n_p being the plasma density, e being the elementary charge, m_e being the electron mass, and ϵ_0 being the vacuum electric permittivity. Note that to lowest order, v_f is equal to the group velocity of the ionizing laser in plasma, giving $\beta_f \approx (1-\omega_p^2/\omega_{\rm ion}^2)^{1/2}$ and $\gamma_f \approx \omega_{\rm ion}/\omega_p$.

In the IF frame, the problem becomes the interaction of a LG laser pulse with a stationary plasma boundary. We are interested in the underdense plasma case ($\omega_p < \omega'_i$) where the incident laser will enter the plasma. According to the plasma dispersion relation, the transmitted wave has a frequency of $\omega'_t = \omega'_i$, wave number of $k'_t = \sqrt{\omega_t'^2 - \omega_p^2}/c$, and phase velocity of $v'_t = \omega'_t/k'_t$. Since the plasma has an azimuthally varying thickness for $d \neq 0$, the phase front of the transmitted wave will undergo a similar azimuthal modulation. At time t'_0, the phase front position z'_0 of such a wave can be given by (see Supplemental Material, Note 2, for detailed derivations)

$$z'_0(t'_0,\phi') = -v'_t t'_0 + \frac{2\pi-\phi'}{2\pi}\gamma_f d \times (1 - v'_t/c) - l'_i(\phi' - 2\pi)/k'_t. \tag{2}$$

For the transmitted wave $E'_{t,x} \propto \exp(-ik'_t z' - i\omega'_t t' - il'_t\phi')$, the phase front is the surface of the constant phase, i.e., $k'_t z'_0(t'_0,\phi') + \omega'_t t'_0 + l'_t\phi' = \text{const}$, giving $l'_t = l'_i + \frac{k'_t\gamma_f d}{2\pi}(1 - v'_t/c)$.

Upon Lorentz transforming back to the laboratory frame, the transmitted frequency and wave number can be calculated as $\omega_t = \gamma_f(\omega'_t - v_f k'_t)$ and $k_t = \gamma_f(k'_t - \omega'_t\beta_f/c)$. In the underdense limit, ω_t and k_t can be approximated as $\omega_t \approx \omega_i(1+\frac{n_p}{4n_{ic}})$ and $k_t \approx k_i(1-\frac{n_p}{4n_{ic}})$, with n_{ic} being the critical density of the incident laser. When $n_p < 4n_{ic}$, $k_t > 0$ and the transmitted wave moves forward in the laboratory frame with $E_{t,x} \propto \exp(-ik_t z - i\omega_t t - il_t\phi)$, where $l_t = l'_t \approx l_i - \frac{d}{\lambda_i}\times\frac{n_p}{4n_{ic}}$. However, when $n_p > 4n_{ic}$, $k_t < 0$ and the transmitted wave actually travels backwards in the laboratory frame (see Fig. 1) with $E_{t,x} \propto \exp(-i|k_t|z + i\omega_t t - il_t\phi)$, where $l_t = -l'_t \approx \frac{d}{\lambda_i}\times\frac{n_p}{4n_{ic}} - l_i$. The frequency-upshifted transmitted wave is an optical vortex, and its OAM mode depends on l_i, d, and n_p, which hence can be manipulated by tuning these parameters. Note that even for the planar IF ($d = 0$), the transmitted OAM mode can be tuned from l_i to $-l_i$ by simply changing n_p from $<4n_{ic}$ to $>4n_{ic}$. In addition, for the helical IF ($d \neq 0$), even though the incident laser is Gaussian mode without OAM ($l_i = 0$), a transmitted laser with variable OAM can still be obtained.

We now explain how the static magnetic vortex is generated. In the IF frame, an electron moving in the plasma region obeys the equation of motion due to the transmitted wave

$$\begin{aligned} -\frac{dv'_{e,x}}{dt'} &= \frac{e}{m_e}(E'_{t,x} - v_f B'_{t,x}) \\ &= \frac{e}{m_e}\left(1 - \frac{k'_t v_f}{\omega'_t}\right)E'_{t,x}(z'=0,t'=0,\phi'=0) \\ &\quad\times\exp(-ik'_t z' - \omega'_t t' - il'_t\phi'), \end{aligned} \tag{3}$$

where $v'_{e,x}$ is the electron velocity in the x direction. Note that here, $\frac{dv'_{e,x}}{dt'} = \frac{\partial v'_{e,x}}{\partial t'} - v_f\frac{\partial v'_{e,x}}{\partial z'}$. Integrating back over the orbit of the electron, and imposing the initial condition that the electron is born (ionized) with $v'_{e,x} = 0$ at $z' = z'_f(\phi')$, time $t' + \frac{z'-z'_f(\phi')}{v_f}$, and azimuthal angle ϕ', we can obtain

$$\begin{aligned} v'_{e,x} &= \frac{ieE'_{t,x}(z'=0,t'=0,\phi'=0)}{m_e\omega'_t} \\ &\quad\times\Bigg\{\exp(-ik'_t z' - i\omega'_t t' - il'_t\phi') \\ &\quad - \exp\Bigg[-ik'_m z' - i\omega'_t t' - i\left(l'_t + \frac{k'_m - k'_t}{2\pi}\gamma_f d\right)\phi' \\ &\quad + i(k'_m - k'_t)\gamma_f d\Bigg]\Bigg\}, \end{aligned} \tag{4}$$

where $k'_m = \omega'_t/v_f$. The current density J'_x is then given by $J'_x = -en'_e v'_{e,x}$. The first term in Eq. (4) generates the current $J'_{t,x}$ associated with the transmitted wave, while the second term leads to the current $J'_{m,x}$ associated with the magnetic vortex. When Lorentz transformed back to the laboratory frame by using $z' = \gamma_f(z - \beta_f ct)$, $t' = \gamma_f(t - \beta_f z/c)$, and $\phi' = \phi$, $J_{m,x}$ is given by

$$J_{m,x} \propto \exp(-ik_m z - il_m\phi), \tag{5}$$

where $k_m = k_i(1+\frac{1}{\beta_f})$ and $l_m = l'_t + \frac{k'_m - k'_t}{2\pi}\gamma_f d = l_i + \frac{d}{\beta_f\lambda_i}$. Note that Eq. (5) can also be derived directly in the laboratory frame (see Supplemental Material, Note 3, for details). As shown in Eq. (5), $J_{m,x}$ is independent of t and dependent on ϕ. After the transmitted wave exits the plasma, only $J_{m,x}$ exists in the plasma since $J_{t,x} \approx 0$. By solving Ampère's law, we obtain the generated magnetic field $B_{m,y}$ in the y direction as

$$B_{m,y} = -\mu_0\int J_{m,x}dz \propto \exp\left(-ik_m z - il_m\phi - i\frac{\pi}{2}\right), \tag{6}$$

where μ_0 is the vacuum magnetic permeability. $B_{m,y}$ is a magnetostatic (independent of t) vortex with wave number of $k_m \approx 2k_i$, wavelength of $\lambda_m \approx \lambda_i/2$, and topological charge of $l_m \approx l_i + \frac{d}{\lambda_i}$. By varying the incident OAM mode l_i and/or the IF parameter d, l_m can be tuned.

We note that although the theoretical formulas presented above, especially l_m and l_t, are derived in the planar IF or the first-order helical IF case, they can also be applied to the high-order helical IF ($|\Delta l_{\rm ion}| > 1$) case when $\frac{d}{\Delta l_{\rm ion}\lambda_i}$ and $\frac{d}{\Delta l_{\rm ion}\lambda_i}\times\frac{n_p}{4n_{ic}}$ are integers. We summarize the key analytical results in Table I.

To verify the above analysis, we perform a series of 3D PIC simulations using the code OSIRIS. In the planar IF case shown in Fig. 1(a), the IF is formed via laser ionization of helium gas by a linearly y-polarized Gaussian pulse with a wavelength of 400 nm, full width at half maximum (FWHM)

TABLE I. Summary of the key theoretical results.

	Magnetic vortex	Optical vortex
Frequency	$\omega_m = 0$	$\omega_t \approx \omega_i\left(1 + \frac{n_p}{4n_{ic}}\right)$
Wave number	$k_m \approx 2k_i$	$k_t \approx k_i\left(1 - \frac{n_p}{4n_{ic}}\right)$
Topological charge	$l_m \approx l_i + \frac{d}{\lambda_i}$	$l_t \approx l_i - \frac{d}{\lambda_i}\frac{n_p}{4n_{ic}}$ if $n_p < 4n_{ic}$
		$l_t \approx \frac{d}{\lambda_i}\frac{n_p}{4n_{ic}} - l_i$ if $n_p > 4n_{ic}$

duration of 20 fs, focal spot size of 250 μm, and peak intensity of 7.5×10^{15} W/cm^2. The outermost electron of the helium atom can be ionized, and the generated plasma has a density of $n_p = 1 \times 10^{20}$ cm^{-3}. The incident linearly x-polarized CO_2 $LG_{0,1}$ laser ($l_i = 1$) has a wavelength of $\lambda_i = 10$ μm, a duration of 0.4 ps (flat-top temporal profile), a focal spot size of 100 μm, and a peak intensity of 5×10^{14} W/cm^2, which is below the tunneling ionization threshold of the outermost electron of helium. The dimensions of the 3D simulation box are $80 \times 400 \times 400$ μm^3, divided by $4400 \times 1000 \times 1000$ cells along the z, x, and y directions, respectively (see Supplemental Material, Note 4, for additional details of the numerical setup). Since $n_p > 4n_{ic}$ (here, $n_{ic} = 1.11 \times 10^{19}$ cm^{-3}), we find that the transmitted wave moves backwards with a vacuum wavelength of 3 μm (in good agreement with the theoretical calculation $\lambda_t = 2\pi c/\omega_t$) and an OAM mode number of $l_t = -1$ [see the optical vortex in Fig. 1(a)].

Figure 3 illustrates the 3D isosurface distribution [Fig. 3(a)] and corresponding slices [Figs. 3(c)–3(e)] of the generated magnetic vortex $B_{m,y}$, where the $LG_{0,1}$-like ($l_m = 1$) vortex structure is clear. The magnetic field amplitude is quite large, about 2.85 MG (285 T). The current density $J_{m,x}$ supporting the magnetic field is shown in Fig. 3(b), which also features a helical isosurface distribution. Both $J_{m,x}$ and $B_{m,y}$ have a wavelength of $\lambda_m \approx \lambda_i/2 \approx 5$ μm. As shown in Eqs. (5) and (6), the phase difference of $B_{m,y}$ relative to $J_{m,x}$ is $\pi/2l_m$, which can be readily seen from the comparison of Figs. 3(c)–3(e) and Figs. 3(f)–3(h). In addition, such a magnetic vortex can last for a relatively long time (~10 ps; see Supplemental Material, Note 5).

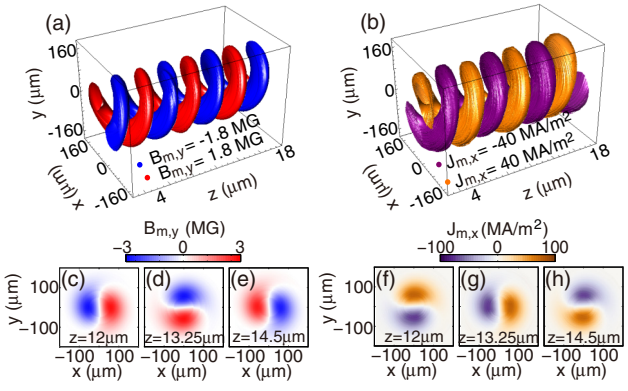

FIG. 3. Simulated isosurfaces of $B_{m,y}$ (a) and $J_{m,x}$ (b) through the interaction of a $LG_{0,1}$ CO_2 laser with a planar IF. (c)–(e) The slices of $B_{m,y}$ at $z = 12$ μm (c), 13.25 μm (d), and 14.5 μm (e). (f)–(h) The slices of $J_{m,x}$ at $z = 12$ μm (f), 13.25 μm (g), and 14.5 μm (h). Note that every two adjacent slices are separated by $\lambda_m/4 = 1.25$ μm.

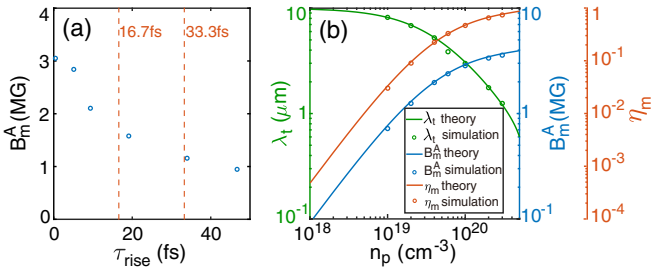

FIG. 4. The magnetic vortex amplitude B_m^A vs the IF rise time $\tau_{\rm rise}$ for $n_p = 1 \times 10^{20}$ cm^{-3}. (b) The transmitted vacuum wavelength λ_t, the amplitude B_m^A, and the energy conversion efficiency η_m vs n_p.

The above argument is valid if the rise time $\tau_{\rm rise}$ of the IF is short compared with half the period $0.5\lambda_i/c$ of the incident CO_2 laser. In our simulations, the helium gas is ionized by the 400-nm laser in just ~6 fs, which is much smaller than $0.5\lambda_i/c \approx 16.7$ fs. If $\tau_{\rm rise} > 0.5\lambda_i/c$, the plasma electrons born in adjacent half cycles can have velocities in the opposite direction, leading to a decrease in the plasma current and magnetic field amplitude [Fig. 4(a)].

In the case of an ideal (instantaneously generated) IF, the transmission coefficient κ_t and magnetic field coefficient κ_m can be easily obtained, which are first calculated in the IF frame by matching electric and magnetic fields at the vacuum-plasma boundary and then transformed back to the laboratory frame [15]. These two coefficients are given by $\kappa_t \equiv \frac{E_t^A}{E_i^A} = \frac{2}{1+\sqrt{\delta}}$ and $\kappa_m \equiv \frac{B_m^A}{B_i^A} = 2\beta_f \frac{1-\sqrt{\delta}}{1-\beta_f\sqrt{\delta}}$, where E_t^A, E_i^A, B_m^A, and B_i^A are the amplitudes of the transmitted electric field, incident electric field, generated static magnetic field, and incident magnetic field in the laboratory frame, respectively, and $\delta = 1 - n_p/[(1+\beta_f)^2\gamma_f^2 n_{ic}]$. In the underdense limit, κ_t approaches unity and the energy conversion efficiency from the incident laser to the transmitted wave is $\eta_t \approx \lambda_t/\lambda_i$. Similarly, the energy conversion efficiency from the incident laser to the static magnetic field is $\eta_m \approx \kappa_m^2/4$. All these quantities are dependent on the plasma density n_p. We have run 3D OSIRIS simulations to show the dependence of λ_t, $B_m^A \equiv \kappa_m B_i^A$, and η_m on n_p using the CO_2 laser parameters corresponding to Fig. 3 ($B_i^A \approx 2.05$ MG), as shown in Fig. 4(b). Good agreement between theory and simulation has been achieved. The transmitted vacuum wavelength λ_t decreases with an increase in n_p and can be tuned in the spectral range 1–10 μm by simply tuning n_p. For high densities, substantial wavelength downshifts (frequency upshifts) occur. Meanwhile, κ_m approaches 1.9, B_m^A approaches 3.9 MG, and η_m approaches 0.9, meaning that 90% of the incident CO_2 laser energy remains stored in the magnetic vortex.

Next, we present the simulation results for the helical IF. Here, a first-order LS with parameters identical to those of Fig. 2(a) is used to ionize helium and generate a first-order helical IF [Fig. 2(b)] with $d \approx \lambda_i = 10$ μm and $n_p = 8n_{ic} = 8.9 \times 10^{19}$ cm^{-3}. The incident LG_{0,l_i} CO_2 laser has the same geometrical parameters as those used in Fig. 3. When it has an OAM mode of $l_i = 1$, the generated magnetic vortex features a double-twisted $LG_{0,2}$-like helical structure with $l_m \approx l_i + \frac{d}{\lambda_i} = 2$ [Figs. 5(a) and 5(c)]. We measure the mode purity by azimuthal modal decomposition, and the results show that ~97% of the energy is contained in the desired $l_m = 3$ mode

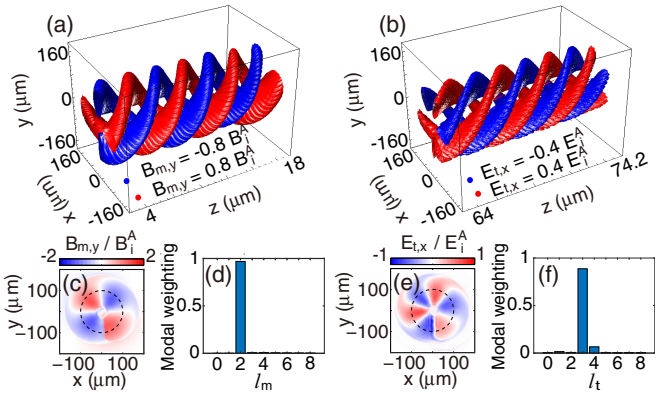

FIG. 5. Simulation results of magnetic or optical vortex generation through the collision of a LG_{0,l_i} CO_2 laser with a first-order helical IF. (a) and (c) show the isosurface and corresponding slice of the magnetic vortex $B_{m,y}$ when $l_i = 1$. (b) and (e) show the isosurface and corresponding slice of the optical vortex $E_{t,x}$ when $l_i = -1$. (d) and (f) show the azimuthal decomposition results of the magnetic [corresponding to (c)] and optical [corresponding to (e)] vortices at a radius of $r = \sqrt{x^2 + y^2} = 100$ μm (dashed circle), respectively.

[Fig. 5(d)]. Meanwhile, the transmitted optical vortex moves backwards with an OAM mode of $l_t \approx \frac{d}{\lambda_i} \times \frac{n_p}{4n_{ic}} - l_i = 1$ [see the optical vortex in Fig. 1(d)]. If l_i is changed from 1 to -1, the generated magnetic field structure will have a planar topology with $l_m = 0$. However, the OAM mode of the transmitted optical vortex will be increased to $l_t \approx \frac{d}{\lambda_i} \times \frac{n_p}{4n_{ic}} - l_i = 3$, as shown in Figs. 5(b) and 5(e), where a triple-twisted $LG_{0,3}$-like helical structure can be clearly seen. The azimuthal mode purity reaches ∼89% [Fig. 5(f)].

In addition to the first-order LS, we also utilize a second-order LS with the same parameters as those of Fig. 2(d) to generate a second-order helical IF [Fig. 2(e)] with $d \approx 2\lambda_i = 20$ μm and $n_p = 8n_{ic} = 8.9 \times 10^{19}$ cm^{-3}. When the same $LG_{0,1}$ CO_2 laser impinges on this IF, both the generated magnetic and optical vortices have a triple-twisted $LG_{0,3}$-like structure with $l_m \approx l_i + \frac{d}{\lambda_i} = 3$ [Fig. 6(a)] and $l_t \approx \frac{d}{\lambda_i} \times \frac{n_p}{4n_{ic}} - l_i = 3$ [Fig. 6(c)], respectively. Both mode purities exceed 90%, as shown in Figs. 6(b) and 6(d). Furthermore, by tuning d and/or n_p, noninteger l_m and l_t values can also be obtained, where the magnetic or optical vortices have complicated phase structures and unique features [52] (see Supplemental Material, Note 6, for examples of noninteger magnetic vortices).

Such ultrashort-wavelength, perfectly periodic, and long-lifetime magnetic vortices can be used as ultracompact spiral undulators for the production of high-power super-radiant x rays with OAM. Since both the electron motion and the properties of radiation in such spiral undulators are different from those in conventional planar undulators, we describe this new physics through large-scale 2D and 3D PIC simulations.

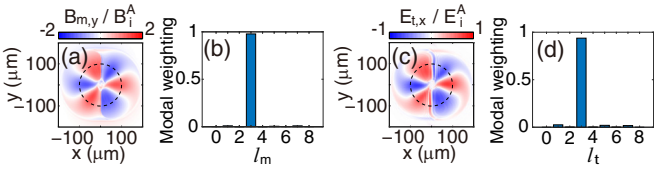

FIG. 6. Simulation results of magnetic or optical vortex generation through the collision of a $LG_{0,1}$ CO_2 laser with a second-order helical IF. (a) and (c) show the slice plots of the magnetic vortex $B_{m,y}$ and optical vortex $E_{t,x}$, respectively. (b) and (d) show the azimuthal decomposition results of the magnetic [corresponding to (a)] and optical [corresponding to (b)] vortices at a radius of $r = 100$ μm (dashed circle), respectively.

Taking the generated $LG_{0,1}$-like ($l_m = 1$) magnetic vortex with a wavelength of $\lambda_m = 5$ μm, an amplitude of $B_m^A = 3.5$ MG, and a normalized undulator parameter of $K = 9.34 B_m^A$ (MG) × λ_m (mm) = 0.1637 as an example, simulations show that by using a 68-pC electron beam with a relativistic factor of $\gamma_b = 50$ and planar prebunching (bunching factor of 0.2), coherent vortex x-ray radiation with a wavelength of $\lambda_r = \lambda_m(1 + K^2/2)/2\gamma_b^2 \approx 1.01$ nm and power of ∼1 MW could be emitted from such a spiral undulator of just ∼1 cm in length. The OAM mode number of the radiation l_r is the opposite of l_m, i.e., $l_r = -l_m = -1$, and therefore can be further manipulated by tuning l_m (see Supplemental Material, Note 7, for details).

Note that during the radiation process in the spiral undulator, the fluctuation of the magnetic field amplitude will induce a fluctuation in the radiation wavelength. To efficiently generate the OAM x-ray radiation and also to enhance the radiation performance, undulator shaping is preferred, where the magnetic field amplitude is precisely tailored to keep the resonant wavelength constant. In addition to being a magnetic "convertor," the plasma can also serve as a magnetic "shaper" to shape both the longitudinal and transverse amplitude distributions by tailoring the plasma density structure due to the amplitude's strong dependence on the local plasma density (see Supplemental Material, Note 8, for an example of longitudinal tailoring).

In summary, we have proposed a scheme that can efficiently generate multimegagauss magnetic vortices and tunable optical vortices. This scheme is based on the interaction of a LG laser pulse with a tailored relativistic IF. Such magnetic and optical vortices have the potential to be used in numerous applications, such as generation of coherent x rays with OAM.

We are grateful to Dr. Frederico Fiúza. This work was supported by U.S. Department of Energy Grant No. DE-SC0010064 and NSF Grant No. 1734315. The simulations were performed on the NERSC Cori cluster at LBNL.

[1] S. Blundell, *Magnetism in Condensed Matter* (Oxford University Press, New York, 2001).

[2] R. F. Post, R. E. Ellis, F. C. Ford, and M. N. Rosenbluth, Stable Confinement of A High-Temperature Plasma, Phys. Rev. Lett. **4**, 166 (1960).

[3] L. Mestel and L. Spitzer Jr, Star formation in magnetic dust clouds, Mon. Not. R. Astron. Soc. **116**, 503 (1956).

[4] M. G. Haines, Generation of an Axial Magnetic Field from Photon Spin, Phys. Rev. Lett. **87**, 135005 (2001).

[5] Z. Najmudin, M. Tatarakis, A. Pukhov, E. L. Clark, R. J. Clarke, A. E. Dangor, J. Faure, V. Malka, D. Neely, M. I. K. Santala, and K. Krushelnick, Measurements of the Inverse Faraday Effect from Relativistic Laser Interactions with an Underdense Plasma, Phys. Rev. Lett. **87**, 215004 (2001).

[6] S. Ali, J. R. Davies, and J. T. Mendonca, Inverse Faraday Effect with Linearly Polarized Laser Pulses, Phys. Rev. Lett. **105**, 035001 (2010).

[7] Y. Shi, J. Vieira, R. M. G. M. Trines, R. Bingham, B. F. Shen, and R. J. Kingham, Magnetic Field Generation in Plasma Waves Driven by Copropagating Intense Twisted Lasers, Phys. Rev. Lett. **121**, 145002 (2018).

[8] R. Nuter, Ph. Korneev, I. Thiele, and V. Tikhonchuk, Plasma solenoid driven by a laser beam carrying an orbital angular momentum, Phys. Rev. E **98**, 033211 (2018).

[9] S. Sederberg, F. Kong, and P. B. Corkum, Tesla-Scale Terahertz Magnetic Impulses, Phys. Rev. X **10**, 011063 (2020).

[10] A. Longman and R. Fedosejevs, Kilo-tesla axial magnetic field generation with high intensity spin and orbital angular momentum beams, Phys. Rev. Res. **3**, 043180 (2021).

[11] S. C. Wilks, W. L. Kruer, M. Tabak, and A. B. Langdon, Absorption of Ultra-Intense Laser Pulses, Phys. Rev. Lett. **69**, 1383 (1992).

[12] R. N. Sudan, Mechanism for the Generation of 10^9 G Magnetic Fields in the Interaction of Ultraintense Short Laser Pulse with an Overdense Plasma Target, Phys. Rev. Lett. **70**, 3075 (1993).

[13] M. Tatarakis, I. Watts, F. N. Beg, E. L. Clark, A. E. Dangor, A. Gopal, M. G. Haines, P. A. Norreys, U. Wagner, M.-S. Wei, M. Zepf, and K. Krushelnick, Measuring huge magnetic fields, Nature (London) **415**, 280 (2002).

[14] M. Lampe, E. Ott, and J. H. Walker, Interaction of electromagnetic waves with a moving ionization front, Phys. Fluids **21**, 42 (1978).

[15] W. B. Mori, Generation of tunable radiation using an underdense ionization front, Phys. Rev. A **44**, 5118 (1991).

[16] F. Fiuza, L. O. Silva, and C. Joshi, High-brilliance synchrotron radiation induced by the plasma magnetostatic mode, Phys. Rev. ST Accel. Beams **13**, 080701 (2010).

[17] C. Zhang, Y. Zhang, X. Yuan, S. Lu, J. Zhang, A. Narayan, Y. Liu, H. Zhang, Z. Ni, R. Liu, E. S. Choi, A. Suslov, S. Sanvito, L. Pi, H.-Z. Lu, A. C. Potter, and F. Xiu, Quantum Hall effect based on Weyl orbits in Cd_3As_2, Nature (London) **565**, 331 (2019).

[18] E. Hemsing, A. Marinelli, and J. B. Rosenzweig, Generating Optical Orbital Angular Momentum in a High-Gain Free-Electron Laser at the First Harmonic, Phys. Rev. Lett. **106**, 164803 (2011).

[19] E. Hemsing, A. Knyazik, M. Dunning, D. Xiang, A. Marinelli, C. Hast, and J. B. Rosenzweig, Coherent optical vortices from relativistic electron beams, Nat. Phys. **9**, 549 (2013).

[20] D. G. Grier, A revolution in optical manipulation, Nature (London) **424**, 810 (2003).

[21] M. Padgett and R. Bowman, Tweezers with a twist, Nat. Photonics **5**, 343 (2011).

[22] M. Zürch, C. Kern, P. Hansinger, A. Dreischuh, and Ch. Spielmann, Strong-field physics with singular light beams, Nat. Phys. **8**, 743 (2012).

[23] C. Hernández-García, A. Picón, J. S. Román, and L. Plaja, Attosecond Extreme Ultraviolet Vortices from High-Order Harmonic Generation, Phys. Rev. Lett. **111**, 083602 (2013).

[24] G. Gariepy, J. Leach, K. T. Kim, T. J. Hammond, E. Frumker, R. W. Boyd, and P. B. Corkum, Creating High-Harmonic Beams with Controlled Orbital Angular Momentum, Phys. Rev. Lett. **113**, 153901 (2014).

[25] X. Zhang, B. Shen, Y. Shi, X. Wang, L. Zhang, W. Wang, J. Xu, L. Yi, and Z. Xu, Generation of Intense High-Order Vortex Harmonics, Phys. Rev. Lett. **114**, 173901 (2015).

[26] M.-T. Horikawa, A. Ogawa, K. Miyamoto, T. Yusufu, and T. Omatsu, Handedness control in a tunable midinfrared (6.0–12.5 μm) vortex laser, J. Opt. Soc. Am. B **32**, 2406 (2015).

[27] S. Araki, K. Ando, K. Miyamoto, and T. Omatsu, Ultra-widely tunable mid-infrared (6–18 μm) optical vortex source, Appl. Opt. **57**, 620 (2018).

[28] J. Zhang, J. Liu, L. Shen, L. Zhang, J. Luo, J. Liu, and S. Yu, Mode-division multiplexed transmission of wavelength-division multiplexing signals over a 100-km single-span orbital angular momentum fiber, Photonics Res. **8**, 1236 (2020).

[29] K. Sueda, G. Miyaji, N. Miyanaga, and M. Nakatsuka, Laguerre-Gaussian beam generated with a multilevel spiral phase plate for high intensity laser pulses, Opt. Express **12**, 3548 (2004).

[30] L. Marrucci, C. Manzo, and D. Paparo, Optical Spin-to-Orbital Angular Momentum Conversion in Inhomogeneous Anisotropic Media, Phys. Rev. Lett. **96**, 163905 (2006).

[31] L. Marrucci, The q-plate and its future, J. Nanophotonics **7**, 078598 (2013).

[32] A. Forbes, A. Dudley, and M. McLaren, Creation and detection of optical modes with spatial light modulators, Adv. Opt. Photonics **8**, 200 (2016).

[33] M. I. Bakunov, A. V. Maslov, A. L. Novokovskaya, N. Yugami, and Y. Nishida, Interaction of an electromagnetic wave with a suddenly stopped ionization front, Phys. Rev. E **66**, 026404 (2002).

[34] C. H. Lai, T. C. Katsouleas, W. B. Mori, and D. Whittum, Frequency upshifting by an ionization front in a magnetized plasma, IEEE Trans. Plasma Sci. **21**, 45 (1993).

[35] W. B. Mori, T. Katsouleas, J. M. Dawson, and C. H. Lai, Conversion of dc Fields in a Capacitor Array to Radiation by a Relativistic Ionization Front, Phys. Rev. Lett. **74**, 542 (1995).

[36] M. I. Bakunov and A. V. Maslov, Frequency upshifting of electromagnetic radiation via oblique incidence on an ionization front, IEEE Trans. Plasma Sci. **27**, 655 (1999).

[37] J. M. Dias, N. C. Lopes, L. O. Silva, G. Figueira, and J. T. Mendonça, Two-dimensional collision of probe photons with relativistic ionization fronts, Phys. Rev. E **65**, 036404 (2002).

[38] C. J. Joshi, C. E. Clayton, K. Marsh, D. B. Hopkins, A. Sessler, and D. Whittum, Demonstration of the frequency upshifting of microwave radiation by rapid plasma creation, IEEE Trans. Plasma Sci. **18**, 814 (1990).

[39] R. L. Savage, C. Joshi, and W. B. Mori, Frequency Upconversion of Electromagnetic Radiation Upon Transmission into an Ionization Front, Phys. Rev. Lett. **68**, 946 (1992).

[40] R. L. Savage, R. P. Brogle, W. B. Mori, and C. Joshi, Frequency upshifting and pulse compression via underdense relativistic ionization fronts, IEEE Trans. Plasma Sci. **21**, 5 (1993).

[41] C. H. Lai, R. Liou, T. C. Katsouleas, P. Muggli, R. Brogle, C. Joshi, and W. B. Mori, Demonstration of Microwave

Generation from a Static Field by a Relativistic Ionization Front in a Capacitor Array, Phys. Rev. Lett. **77**, 4764 (1996).

[42] P. Muggli, R. Liou, J. Hoffman, T. Katsouleas, and C. Joshi, Generation of ultrashort, discrete spectrum microwave pulses using the dc to ac radiation converter, Appl. Phys. Lett. **72**, 19 (1998).

[43] N. Yugami, K. Fujita, T. Higashiguchi, and Y. Nishida, Experimental observation of short microwave generation via relativistic ionization front produced by CO_2 laser, Jpn. J. Appl. Phys. **37**, 688 (1998).

[44] T. Higashiguchi, N. Yugami, H. Okabe, T. Niiyama, E. Takahashi, H. Ito, and Y. Nishida, Emission of short microwave pulse radiated by interaction between periodic static electric field and relativistic ionization front, Jpn. J. Appl. Phys. **38**, L527 (1999).

[45] J. M. Dias, C. Stenz, N. Lopes, X. Badiche, F. Blasco, A. Dos Santos, L. Oliveira e Silva, A. Mysyrowicz, A. Antonetti, and J. T. Mendonça, Experimental Evidence of Photon Acceleration of Ultrashort Laser Pulses in Relativistic Ionization Fronts, Phys. Rev. Lett. **78**, 4773 (1997).

[46] J. M. Dias, N. C. Lopes, L. O. Silva, G. Figueira, J. T. Mendonça, C. Stenz, F. Blasco, A. Dos Santos, and A. Mysyrowicz, Photon acceleration of ultrashort laser pulses by relativistic ionization fronts, Phys. Rev. E **66**, 056406 (2002).

[47] L. Allen, M. W. Beijersbergen, R. J. C. Spreeuw, and J. P. Woerdman, Orbital angular momentum of light and the transformation of Laguerre-Gaussian laser modes, Phys. Rev. A **45**, 8185 (1992).

[48] G. Pariente and F. Quéré, Spatio-temporal light springs: extended encoding of orbital angular momentum in ultrashort pulses, Opt. Lett. **40**, 2037 (2015).

[49] J. Vieira, J. T. Mendonça, and F. Quéré, Optical Control of the Topology of Laser-Plasma Accelerators, Phys. Rev. Lett. **121**, 054801 (2018).

[50] R. A. Fonseca, L. O. Silva, F. S. Tsung, V. K. Decyk, W. Lu, C. Ren, W. B. Mori, S. Deng, S. Lee, T. Katsouleas, and J. C. Adam, Osiris: A three-dimensional, fully relativistic particle in cell code for modeling plasma based accelerators, in *Computational Science—ICCS 2002* (Springer, Berlin, 2002), pp. 342–351.

[51] See Supplemental Material at http://link.aps.org/supplemental/10.1103/PhysRevResearch.5.L012011 for detailed parameters and derivations, additional details of the numerical setup, examples of noninteger magnetic vortices, simulations of OAM x-ray generation, and an example of longitudinal tailoring, among other things.

[52] M. V. Berry, Optical vortices evolving from helicoidal integer and fractional phase steps, J. Opt. A: Pure Appl. Opt. **6**, 259 (2004).